MIT Libraries | DSpace@MIT

MIT Open Access Articles

Time-resolved imaging of near-fields in THz antennas and direct quantitative measurement of field enhancements

The MIT Faculty has made this article openly available. ***Please share*** how this access benefits you. Your story matters.

Citation: Werley, Christopher A. et al. "Time-resolved Imaging of Near-fields in THz Antennas and Direct Quantitative Measurement of Field Enhancements." Optics Express 20.8 (2012): 8551.
© 2012 OSA

As Published: http://dx.doi.org/10.1364/OE.20.008551

Publisher: Optical Society of America

Persistent URL: http://hdl.handle.net/1721.1/71939

Version: Final published version: final published article, as it appeared in a journal, conference proceedings, or other formally published context

Terms of Use: Article is made available in accordance with the publisher's policy and may be subject to US copyright law. Please refer to the publisher's site for terms of use.

Massachusetts Institute of Technology

Time-resolved imaging of near-fields in THz antennas and direct quantitative measurement of field enhancements

Christopher A. Werley,[1] Kebin Fan,[2] Andrew C. Strikwerda,[3] Stephanie M. Teo,[1] Xin Zhang,[2] Richard D. Averitt,[3] and Keith A. Nelson[1,*]

[1]*Department of Chemistry, Massachusetts Institute of Technology, Cambridge, Massachusetts 02139 USA*
[2]*Department of Mechanical Engineering, Boston University, Boston, Massachusetts 02215 USA*
[3]*Department of Physics, Boston University, Boston, Massachusetts 02215 USA*
[*]*kanelson@mit.edu*

Abstract: We investigate the interaction between terahertz waves and resonant antennas with sub-cycle temporal and $\lambda/100$ spatial resolution. Depositing antennas on a $LiNbO_3$ waveguide enables non-invasive electro-optic imaging, quantitative field characterization, and direct measurement of field enhancement (up to 40-fold). The spectral response is determined over a bandwidth spanning from DC across multiple resonances, and distinct behavior is observed in the near- and far-field. The scaling of enhancement and resonant frequency with gap size and antenna length agrees well with simulations.

©2012 Optical Society of America

OCIS codes: (190.4360) Nonlinear optics, devices; (190.7110) Ultrafast nonlinear optics; (300.6495) Spectroscopy, terahertz; (250.5403) Plasmonics.

References and links

1. C. A. Balanis, *Antenna Theory: Analysis and Design*, 3rd ed. (Wiley, 2005).
2. A. Kinkhabwala, Z. Yu, S. Fan, Y. Avlasevich, K. Müllen, and W. E. Moerner, "Large single-molecule fluorescence enhancements produced by a bowtie nanoantenna," Nat. Photonics **3**(11), 654–657 (2009).
3. D. P. Fromm, A. Sundaramurthy, A. Kinkhabwala, P. J. Schuck, G. S. Kino, and W. E. Moerner, "Exploring the chemical enhancement for surface-enhanced Raman scattering with Au bowtie nanoantennas," J. Chem. Phys. **124**(6), 061101 (2006).
4. K. A. Willets and R. P. Van Duyne, "Localized surface plasmon resonance spectroscopy and sensing," Annu. Rev. Phys. Chem. **58**(1), 267–297 (2007).
5. E. Cubukcu, Nanfang Yu, E. J. Smythe, L. Diehl, K. B. Crozier, and F. Capasso, "Plasmonic laser antennas and related devices," IEEE J. Sel. Top. Quantum Electron. **14**(6), 1448–1461 (2008).
6. P. Mühlschlegel, H.-J. Eisler, O. J. F. Martin, B. Hecht, and D. W. Pohl, "Resonant optical antennas," Science **308**(5728), 1607–1609 (2005).
7. P. Ghenuche, S. Cherukulappurath, T. H. Taminiau, N. F. van Hulst, and R. Quidant, "Spectroscopic mode mapping of resonant plasmon nanoantennas," Phys. Rev. Lett. **101**(11), 116805 (2008).
8. D. R. Ward, F. Hüser, F. Pauly, J. C. Cuevas, and D. Natelson, "Optical rectification and field enhancement in a plasmonic nanogap," Nat. Nanotechnol. **5**(10), 732–736 (2010).
9. K. B. Crozier, A. Sundaramurthy, G. S. Kino, and C. F. Quate, "Optical antennas: Resonators for local field enhancement," J. Appl. Phys. **94**(7), 4632–4642 (2003).
10. E. S. Barnard, R. A. Pala, and M. L. Brongersma, "Photocurrent mapping of near-field optical antenna resonances," Nat. Nanotechnol. **6**(9), 588–593 (2011).
11. M. Schnell, A. Garcia-Etxarri, J. Alkorta, J. Aizpurua, and R. Hillenbrand, "Phase-resolved mapping of the near-field vector and polarization state in nanoscale antenna gaps," Nano Lett. **10**(9), 3524–3528 (2010).
12. C. Höppener and L. Novotny, "Antenna-based optical imaging of single Ca^{2+} transmembrane proteins in liquids," Nano Lett. **8**(2), 642–646 (2008).
13. H. Fischer and O. J. F. Martin, "Engineering the optical response of plasmonic nanoantennas," Opt. Express **16**(12), 9144–9154 (2008).
14. A. Bitzer, A. Ortner, and M. Walther, "Terahertz near-field microscopy with subwavelength spatial resolution based on photoconductive antennas," Appl. Opt. **49**(19), E1–E6 (2010).
15. F. Blanchard, A. Doi, T. Tanaka, H. Hirori, H. Tanaka, Y. Kadoya, and K. Tanaka, "Real-time terahertz near-field microscope," Opt. Express **19**(9), 8277–8284 (2011).

#161464 - $15.00 USD Received 13 Jan 2012; revised 21 Mar 2012; accepted 21 Mar 2012; published 28 Mar 2012

16. K. Imura and H. Okamoto, "Reciprocity in scanning near-field optical microscopy: illumination and collection modes of transmission measurements," Opt. Lett. **31**(10), 1474–1476 (2006).
17. S. Mujumdar, A. F. Koenderink, R. Wüest, and V. Sandoghdar, "Nano-optomechanical characterization and manipulation of photonic crystals," IEEE J. Sel. Top. Quantum Electron. **13**(2), 253–261 (2007).
18. K. Wang, D. M. Mittleman, N. C. J. van der Valk, and P. C. M. Planken, "Antenna effects in terahertz apertureless near-field optical microscopy," Appl. Phys. Lett. **85**(14), 2715–2717 (2004).
19. T. Feurer, N. S. Stoyanov, D. W. Ward, J. C. Vaughan, E. R. Statz, and K. A. Nelson, "Terahertz polaritonics," Annu. Rev. Mater. Res. **37**(1), 317–350 (2007).
20. T. Feurer, J. C. Vaughan, and K. A. Nelson, "Spatiotemporal coherent control of lattice vibrational waves," Science **299**(5605), 374–377 (2003).
21. K.-H. Lin, C. A. Werley, and K. A. Nelson, "Generation of multicycle terahertz phonon-polariton waves in a planar waveguide by tilted optical pulse fronts," Appl. Phys. Lett. **95**(10), 103304 (2009).
22. N. S. Stoyanov, D. W. Ward, T. Feurer, and K. A. Nelson, "Terahertz polariton propagation in patterned materials," Nat. Mater. **1**(2), 95–98 (2002).
23. P. Peier, S. Pilz, and T. Feurer, "Time-resolved coherent imaging of a THz multilayer response," J. Opt. Soc. Am. B **26**(8), 1649–1655 (2009).
24. R. M. Koehl, S. Adachi, and K. A. Nelson, "Direct visualization of collective wavepacket dynamics," J. Phys. Chem. A **103**(49), 10260–10267 (1999).
25. P. Peier, S. Pilz, F. Müller, K. A. Nelson, and T. Feurer, "Analysis of phase contrast imaging of terahertz phonon-polaritons," J. Opt. Soc. Am. B **25**(7), B70–B75 (2008).
26. Q. Wu, C. A. Werley, K.-H. Lin, A. Dorn, M. G. Bawendi, and K. A. Nelson, "Quantitative phase contrast imaging of THz electric fields in a dielectric waveguide," Opt. Express **17**(11), 9219–9225 (2009).
27. C. A. Werley, Q. Wu, K.-H. Lin, C. R. Tait, A. Dorn, and K. A. Nelson, "Comparison of phase-sensitive imaging techniques for studying terahertz waves in structured $LiNbO_3$," J. Opt. Soc. Am. B **27**(11), 2350–2359 (2010).
28. T. P. Dougherty, G. P. Wiederrecht, and K. A. Nelson, "Impulsive stimulated Raman scattering experiments in the polariton regime," J. Opt. Soc. Am. **9**(12), 2179–2189 (1992).
29. J. H. Kang, D. S. Kim, and Q.-H. Park, "Local capacitor model for plasmonic electric field enhancement," Phys. Rev. Lett. **102**(9), 093906 (2009).
30. B. J. Messinger, K. U. von Raben, R. K. Chang, and P. W. Barber, "Local fields at the surface of noble-metal microspheres," Phys. Rev. B **24**(2), 649–657 (1981).
31. M. A. Seo, A. J. L. Adam, J. H. Kang, J. W. Lee, K. J. Ahn, Q. H. Park, P. C. M. Planken, and D. S. Kim, "Near field imaging of terahertz focusing onto rectangular apertures," Opt. Express **16**(25), 20484–20489 (2008).
32. M. A. Seo, H. R. Park, S. M. Koo, D. J. Park, J. H. Kang, O. K. Suwal, S. S. Choi, P. C. M. Planken, G. S. Park, N. K. Park, Q. H. Park, and D. S. Kim, "Terahertz field enhancement by a metallic nano slit operating beyond the skin-depth limit," Nat. Photonics **3**(3), 152–156 (2009).
33. T. Bartel, P. Gaal, K. Reimann, M. Woerner, and T. Elsaesser, "Generation of single-cycle THz transients with high electric-field amplitudes," Opt. Lett. **30**(20), 2805–2807 (2005).
34. K.-L. Yeh, M. C. Hoffmann, J. Hebling, and K. A. Nelson, "Generation of 10 μJ ultrashort terahertz pulses by optical rectification," Appl. Phys. Lett. **90**(17), 171121 (2007).
35. H. Hirori, A. Doi, F. Blanchard, and K. Tanaka, "Single-cycle terahertz pulses with amplitudes exceeding 1 MV/cm generated by optical rectification in $LiNbO_3$," Appl. Phys. Lett. **98**(9), 091106 (2011).
36. C. A. Werley, S. M. Teo, and K. A. Nelson, "Pulsed laser noise analysis and pump-probe signal detection with a data acquisition card," Rev. Sci. Instrum. **82**(12), 123108 (2011).
37. A. Yariv and P. Yeh, *Photonics: Optical Electronics in Modern Communications*, 6th ed. (Oxford Univ. Press, 2007).
38. C. Thomsen, H. T. Grahn, H. J. Maris, and J. Tauc, "Surface generation and detection of phonons by picosecond light pulses," Phys. Rev. B Condens. Matter **34**(6), 4129–4138 (1986).
39. B. E. A. Saleh and M. C. Teich, *Fundamentals of Photonics*, 2nd ed. (Wiley, 2007).

Antennas, which convert electromagnetic radiation into electrical currents and vice versa, have important applications spanning the electromagnetic spectrum from radio to visible frequencies. The technology is mature at radio and microwave frequencies where antennas are used in mobile telephones, television broadcasting, and many other applications. At these frequencies, study has focused on sending and receiving information [1] and therefore has primarily considered signals far from the internal antenna elements, i.e. in the far-field. More recently, studies at infrared and optical frequencies have focused instead on the antenna's ability to provide field enhancement and subwavelength field localization [2–11]. Antennas have been used in single-molecule fluorescence [2], surface enhanced Raman spectroscopy [3,4], near-field scanning optical microscopy [12], photonic devices [5] and novel nonlinear optics [6–8]. Although near-field signals assume primary interest in these studies, it has proved difficult to quantify electric field amplitudes and enhancements and characterize field profiles around the antenna because of the small length scales and a lack of methods for direct

#161464 - $15.00 USD Received 13 Jan 2012; revised 21 Mar 2012; accepted 21 Mar 2012; published 28 Mar 2012
(C) 2012 OSA

field visualization. It has also been difficult to determine the full spectral response because of the ultra-broad bandwidth required: an antenna resonant in the visible displays important behavior spanning from DC to ultraviolet frequencies. Because of the experimental challenges, most of the understanding of near-field behavior in antennas has relied on simulations that have only been experimentally verified in the far-field. Comparing near-field simulations with experiments is complicated by sample inhomogeneity, surface roughness, and chemical adsorbates; even the ideal case presents challenges because modeling tightly localized fields requires a very fine mesh, while capturing the far-field behavior needs a large simulation volume. In short, quantitative measurement of near-field behavior is critical for validating theoretical methods that will be used in the design of future devices and experiments.

Many experimental studies at THz, infrared, and visible frequencies have tried to characterize fields around resonant antennas [5–11,13–15], but results have not been definitive. Scanning near-field probes yielded high-resolution field maps [5,11,16], but there is strong evidence that scanning tips significantly perturb the fields being measured [16–18]. Nonlinear microscopy at visible frequencies [7] and electro-optic probing at THz frequencies with sub-wavelength resolution [14,15] made it possible to map antenna mode structure without seriously perturbing the system, but the tightly localized, strongly enhanced fields near antenna ends and gaps were not spatially resolved or directly quantified. Recently, photocurrents in an optical antenna were measured [10], but volume-averaging of fields prevents the quantification of near-fields with subwavelength resolution. Another recent study determined field strengths in angstrom-sized gaps between electrodes using tunneling currents [8], but it is difficult to infer antenna behavior from the atomic-scale gaps in these irregularly-shaped structures. Here, we use a THz polaritonics platform [19] to study antennas without perturbing the system or compromising on spatial resolution.

The polaritonics platform allows versatile THz generation [20,21], control [22,23], and time-resolved imaging of THz electric fields [24–27]. Several favorable considerations enable particularly incisive study of antennas and other metallic microstructures using this system. First, because the THz wave propagates in an electro-optic medium, it is possible to directly record its electric field (*E*-field) and thus quantify field enhancement, a capability that has proved difficult in previous experiments. Second, the *E*-field is imaged with an optical probe without the need for a tip or other intrusive element. The spatial resolution is ultimately set by the optical diffraction limit [26,27], which is hundreds of times smaller than the THz wavelength. The temporal resolution is set by the duration of the femtosecond optical probe pulse, which is a small fraction of the THz period. Third, the THz antennas can be deposited directly onto the THz propagation medium with high precision using optical lithography. Finally, facile control over the THz field allows us to initially probe the antennas with broadband THz waves in order to characterize the frequency-dependent response from 0.1 to 2 THz and survey for resonances. We subsequently drive the antennas with multi-cycle THz waves tuned to the antennas' resonant frequencies in order to study the resonant responses in detail and maximize field enhancement. Because of the versatility of the THz polaritonics system and its ability to spatially, temporally, and spectrally resolve the antenna response, it is possible to develop a detailed and scalable understanding of antenna behavior.

#161464 - $15.00 USD Received 13 Jan 2012; revised 21 Mar 2012; accepted 21 Mar 2012; published 28 Mar 2012
(C) 2012 OSA

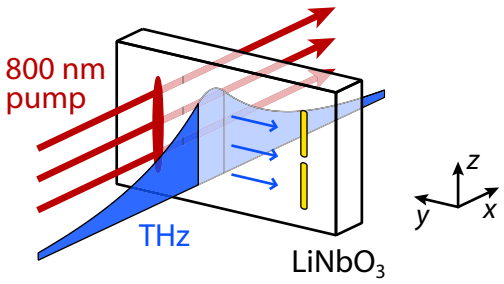

Fig. 1. The experimental pumping geometry. A THz wave is generated by an ultrafast optical pump pulse and guided down the 30 μm thick $LiNbO_3$ slab until its evanescent field interacts with the gold antenna deposited on the surface.

The experimental geometry is shown in Fig. 1. A z-polarized 800 nm, 80-fs pump pulse passes through a thin $LiNbO_3$ slab where it generates a THz response via impulsive stimulated Raman scattering [28]. The optic axis of the $LiNbO_3$ slab is aligned along z, as is the polarization of the generated THz wave. The THz field is wave-guided within the high-index slab, propagating from the generation region to a gold micro-antenna deposited on the crystal surface. The antenna was a pair of half-wave strips aligned end-to-end with a small gap between them, as shown in Fig. 2(a). Strips were chosen because they generate larger enhancements than other geometries [9,13], and the ends were given a smooth, 5 μm radius of curvature so that fields in the gap would be relatively uniform and undistorted by sharp tip effects. The antennas were 150 nm thick gold deposited with optical lithography (see Appendix A). All antennas studied were 10 μm wide, with lengths ranging from 30 to 110 μm and gaps ranging from 2 to 20 μm. Figure 2(b) shows an image of a typical antenna. The white spot in the gap is the reflection of a tightly focused optical beam (see Appendix C, Fig. 8), which was used for recording THz transients in the gap.

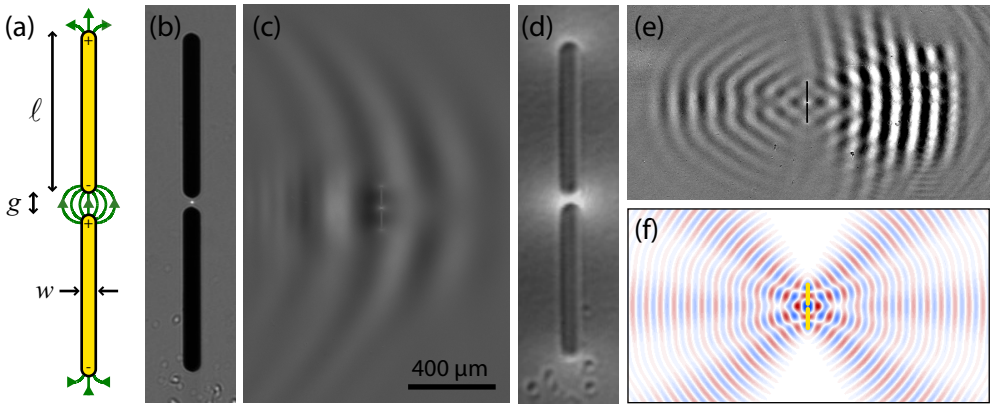

Fig. 2. Antenna design and images of THz fields. (a)-(f) $w = 10\,\mu m$ and $g = 5\,\mu m$. In (b)-(d) $\ell = 94\,\mu m$ and in (e) and (f) $\ell = 110\,\mu m$. (a) The charge distribution and electric field lines (in green) for the lowest antenna mode. (b) An optical image of the antenna. (c) An experimental image of E_z at one moment in time as a rightward-propagating, resonant THz wave interacts with the antenna in (b) (Media 1). (d) A magnified view of (c) with better than 2 μm resolution. (e) The field profile soon after a rightward-propagating THz wave at 760 GHz (the second antenna resonance) has passed the antenna (Media 2). (f) The theoretical wave pattern emitted from a pair of $\ell = 3\lambda/2$ wires in free space.

When driven on resonance, current flow in a half-wave antenna results in a standing wave charge distribution with maxima at the ends of each antenna arm. The antenna pair acts like a small capacitor [29], and the E-field, represented by green lines in Fig. 2(a), is confined and enhanced in the subwavelength gap. To study field localization and mode structure, we

#161464 - $15.00 USD Received 13 Jan 2012; revised 21 Mar 2012; accepted 21 Mar 2012; published 28 Mar 2012
(C) 2012 OSA

excited the antenna on resonance with a multi-cycle THz wave [21] and recorded movies of the wave as it interacted with the antenna using time-resolved, phase-sensitive imaging techniques [26,27] as illustrated in Appendix B, Fig. 7. Figure 2(c)–2(e) are frames from such movies, which show the *z*-component of the propagating THz wave's *E*-field. Figure 2(c) (from Media 1) shows a zoomed-out view of the THz wave tuned to 255 GHz, the frequency of maximum enhancement (see below), as it interacts with the antenna at image center. Figure 2(d) is zoomed in on the antenna. Field enhancement at the antenna ends and even greater enhancement in the gap center is visible, in agreement with the qualitative depiction in Fig. 2(a). Figure 2(e) (from Media 2) shows the more complex $\ell = 3\lambda/2$ antenna mode. The left side of the image shows the field emitted from the antenna just after the rightward propagating THz wave has passed. Figure 2(f) shows the analytically predicted wave pattern emitted from a pair of $3\lambda/2$ wire antennas in a homogeneous dielectric such as free space, with the antenna arms oriented and separated to match experiment [1]. Although there are quantitative differences due to the presence of the high-dielectric slab, the radiation pattern emitted from each antenna arm has two horizontal nodes, and interference generates an *E*-field profile qualitatively consistent with what we observed.

In order to perform spectroscopy on the antennas, we switched from imaging the THz waves to localized detection, which provides a higher signal-to-noise ratio (S/N). We focused the probe beam to a 1 μm diameter spot which could be accurately positioned relative to the sample (see Appendix C) to enable direct probing of the field in the antenna gap. Spectroscopy was performed both in transmission and reflection geometries. Transmission yielded excellent S/N but measured the THz *E*-field averaged through the 30-μm crystal thickness. In contrast, reflection yielded weaker signals but quantitatively measured the *E*-field amplitude directly at the $LiNbO_3$ surface on which the antenna was deposited (see Appendix C).

To find the resonances of the antenna, the structure was interrogated with a broadband THz wave and detected in the optical transmission geometry. We recorded the time-resolved THz transients [Fig. 3(a)] at three locations as shown in the inset of Fig. 3(b): a reference trace far removed from the antenna, a point soon after the THz wave had propagated past the antenna (similar to a typical THz transmission measurement), and directly in the antenna gap as seen in Fig. 2(b). The THz amplitude spectra, calculated by taking the Fourier transforms of the time domain signals, are shown in Fig. 3(b), and the transmission spectra, the ratio of signal and reference, are shown in Fig. 3(c). The spectrum measured after the antenna (orange) shows clear dips, corresponding to transmission minima resulting from resonant modes of the antenna. The two lowest modes ($\ell = \lambda/2$ at 350 GHz and $\ell = 3\lambda/2$ at 860 GHz) are clearly visible. The ratio between these frequencies would be exactly three for an extremely thin wire in a homogeneous dielectric [1], but it is significantly lower here because of the complex geometry (a finite width antenna deposited on a high-index planar waveguide substrate [21,27]).

Behavior in the antenna gap [green traces in Fig. 3] is very different from that measured after the antenna. The amplitude spectrum in Fig. 3(c) reveals a clear and strong enhancement at 255 GHz. The frequency shift between the in-gap enhancement maximum and the maximum scattering frequency (the transmission minimum) is not unexpected, as such a shift has been previously predicted [30] and observed [7] in similar structures. Other notable features of the in-gap spectrum are enhancement down to DC and an amplitude reduction at a higher frequency than the transmission minimum (~490 GHz). The DC enhancement, amplitude reduction, and in-gap enhancement maximum are also present in other antennas with different arm lengths and gap sizes (see Fig. 4 and 5), showing that these are general behaviors for half-wave antennas. They can be understood qualitatively by thinking of the antenna as a damped driven harmonic oscillator, which also has an amplitude maximum that occurs at a lower frequency than the resonant frequency, a DC response that depends only on the resonant frequency and oscillator strength, and a frequency-dependent phase shift (see

#161464 - $15.00 USD Received 13 Jan 2012; revised 21 Mar 2012; accepted 21 Mar 2012; published 28 Mar 2012
(C) 2012 OSA

Appendix D). Above the resonant frequency, the phase shift leads to destructive interference between the driving field and induced response, which is evident in our results as an enhancement minimum with a value less than unity and is responsible for the Fano-like line-shape of the enhancement.

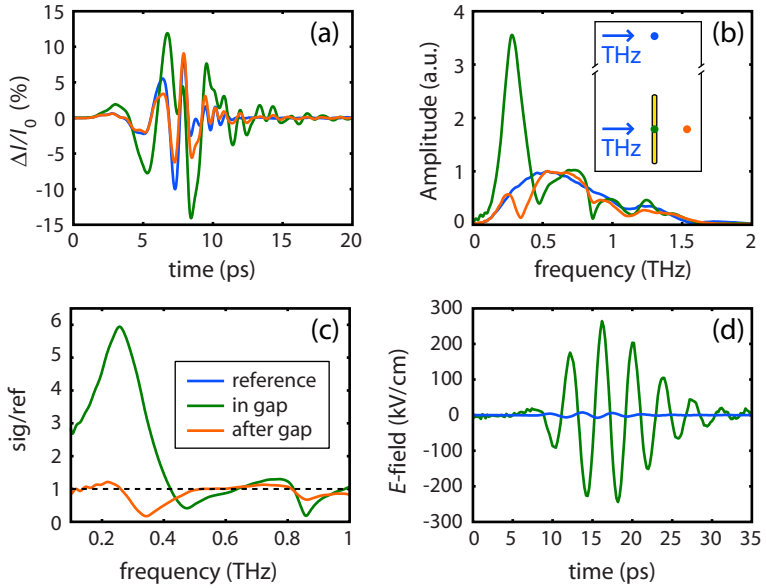

Fig. 3. (a) Time traces of a broadband THz wave measured far above the antenna (blue spot in the inset of (b), the reference field location); ~100 μm after the antenna (orange spot); and directly in the 5 μm antenna gap (green spot). (b) The spectral amplitude of each trace calculated from the Fourier transform of data in (a). (c) The ratio of signal and reference traces shown in (b). (d) The time trace for a multi-cycle reference THz wave (blue) and the enhanced field measured in a 2 μm antenna gap (green).

To further study the lowest frequency $\lambda/2$ mode, which shows the largest E-field enhancement, we excited the antenna with a multi-cycle THz pulse [21] tuned to the frequency of maximum enhancement. THz transients were recorded in reflection to accurately measure the field at the crystal surface and to quantitatively determine the extent of field enhancement around gap center; even higher fields will be present closer to the metal surface. Figure 3(d) shows the reference trace measured far from the antenna (blue) and the trace recorded in a 2 μm antenna gap (green). The peak field strength of 265 kV/cm is enhanced by 35-fold relative to the reference trace, and the peak amplitude enhancement in the Fourier domain is 38-fold. The charge in the metal antenna continues to oscillate after the driving field has decayed away, evidenced by the fact that the trace measured in the gap persists for several cycles longer than the reference trace. This is consistent with a resonator quality factor (Q) slightly greater than one as calculated from the enhancement linewidth. For the peak field strength (265 kV/cm) and 2 μm gap size, the potential drop across the gap is about 60 V. Using an approximation of the capacitance (10^{15} F), we estimate that ~10^6 electrons were driven onto the antenna ends by the incoming THz wave.

To determine the effects of antenna geometry on the antenna response (enhancement, resonant frequency, etc.), we fabricated antennas with different arm lengths and gap sizes. The amplitude ratios between reference traces and scans recorded in and after the gap, like those shown in Fig. 3(c), are shown for each antenna in Fig. 4. In Fig. 4(a) and 4(c), which vary the gap size but keep the antenna arm length constant, the DC offset, maxima, and minima are clearly visible for the first two modes of each antenna. Other than the magnitude of the near-field response, the spectra are nearly independent of gap size. In contrast, the

#161464 - $15.00 USD Received 13 Jan 2012; revised 21 Mar 2012; accepted 21 Mar 2012; published 28 Mar 2012
(C) 2012 OSA

resonant frequencies, linewidths, and peak response depend strongly on antenna length [Figs. 4(b) and 4(d)]. In the 30 μm long antenna [dark green in Fig. 4(b)], for instance, the enhancement is weak and nearly constant for frequencies below ~750 GHz. The 110 μm long antenna [dark purple in Fig. 4(b)], in contrast, is sharply peaked at ~200 GHz and shows much larger enhancements.

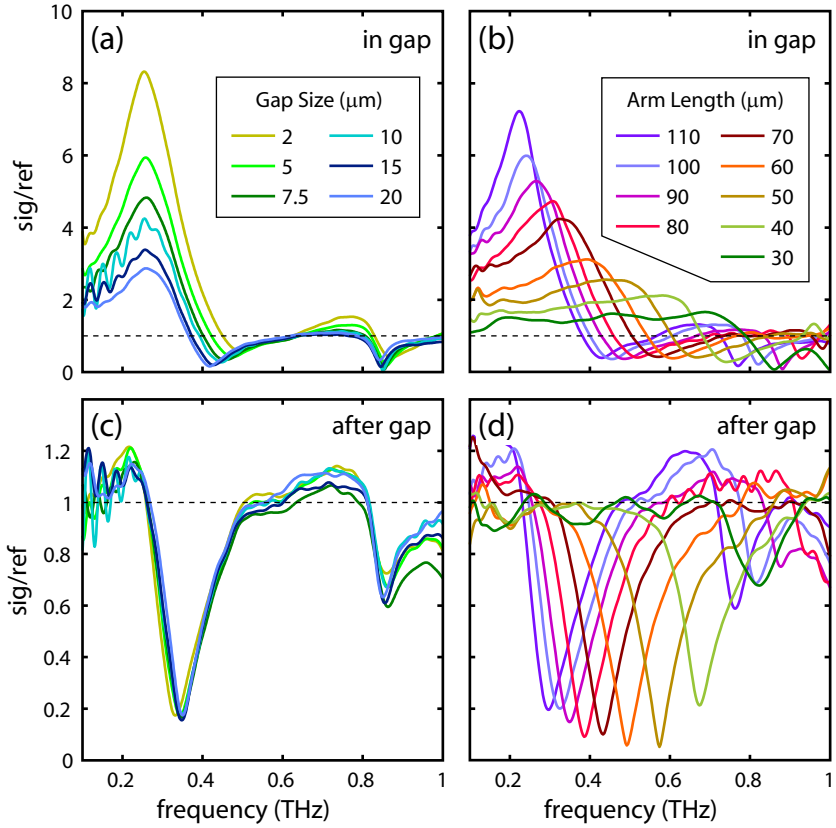

Fig. 4. In-gap enhancement spectra [green dot in Fig. 3(b)] for various antennas are shown in (a) and (b), and transmission spectra [orange dot in Fig. 3(b)] are shown in (c) and (d). (a) and (c) Spectra for a fixed arm length $\ell = 94\,\mu\text{m}$ for different gap sizes. (b) and (d) Spectra for a fixed gap size g = 5 μm for different arm lengths.

To understand the scaling of antenna properties with arm length and gap size, we extracted the frequency at which minimum transmission occurred and the frequency at which maximum enhancement occurred from the traces in Fig. 4. In addition, traces like those in Fig. 3(d) were recorded in reflection for each antenna to quantify the peak field enhancement. Finite difference time domain (FDTD) simulations were performed using the commercial software CST Microwave Studio to corroborate experimental results. Experimental results (solid symbols), simulation results (dashed orange and solid green lines), and simple trend lines (dotted and dot-dashed black) are collected in Fig. 5.

Figure 5(a) shows the frequency of minimum transmission and maximum enhancement for the $\lambda/2$ (lower set of data) and the $3\lambda/2$ (upper set of data) modes. Experiment and simulation show these frequencies are nearly independent of gap size. This lack of dependence indicates that the length of a single antenna arm determines the resonant frequency, and that coupling between antenna arms is weak at these gap sizes. Figure 5(b) shows the frequencies as a function of arm length ℓ for both the $\lambda/2$ and $3\lambda/2$ modes. Large frequency shifts between near- and far-field resonances are clearly visible for all gap sizes and

#161464 - $15.00 USD Received 13 Jan 2012; revised 21 Mar 2012; accepted 21 Mar 2012; published 28 Mar 2012
(C) 2012 OSA

antenna lengths. Experiment and simulation agree that the resonant frequency increases sharply for shorter lengths. Microwave theory predicts that antennas in free space will have maximum scattering at a frequency where the arm length is an integer number of half wavelengths, m, with m odd [1]. We fit the data with a simple one-parameter model: $f_{\text{res}} = c/(n_{\text{eff}}\lambda_{\text{res}}) = mc/(2n_{\text{eff}}\ell)$, where an effective index, n_{eff}, is used to account for the complex sample geometry of an antenna deposited on a subwavelength, high-index substrate. Although it was not possible to fit the peak scattering frequency with a single n_{eff} as was expected, the simple $1/\ell$ fit agrees reasonably well with the frequency of peak enhancement for both the $\lambda/2$ and $3\lambda/2$ modes; the dotted black line in Fig. 5(a) and 5(b) is the resonant frequency predicted for $n_{\text{eff}} = 6.4$, an index that surprisingly is higher than that of the substrate. Even though the theory of microwave antennas is quite mature, it is still important to do careful experiments and modeling to fully understand the behavior of samples with non-ideal geometries.

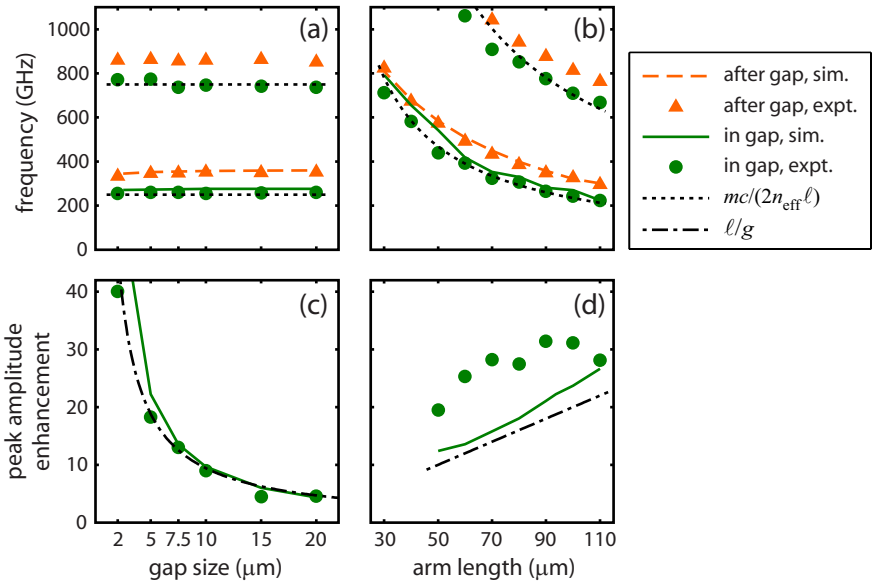

Fig. 5. Trends as a function of gap size for a fixed arm length of 94 μm [(a) and (c)] and as a function of arm length for a fixed gap size of 5 μm [(b) and (d)]. (a) and (b) show the frequency at which the peak enhancement occurred (green) and the frequency of the antenna for which the transmission was minimized (orange).The upper set of data in (a) and (b) (circles and triangles) corresponds to the $3\lambda/2$ antenna mode and the lower data corresponds to the $\lambda/2$ mode. (c) and (d) show the maximum amplitude enhancement in the antenna gap. Green circles are experimental measurements in the gap and orange triangles are experimental measurements after the gap. The solid green (in gap) and dashed orange (after gap) lines are the results of FDTD simulations with the same gap sizes and arm lengths as in the experiments.

Figure 5(c) shows the peak amplitude enhancement (measured in the frequency domain) as a function of gap size. As the gap is decreased, the enhancement increases rapidly. As was discussed previously, at a given instant the antenna can be thought of as a capacitor, where the charge driven onto the ends of the antenna arms by the incoming THz wave is independent of gap size. For smaller gaps, the same voltage drop occurs over a smaller distance, resulting in an increased E-field. Experiment, simulation, and intuitive modeling all indicate that even larger field enhancements would be present in gaps smaller than the ones measured here, consistent with THz enhancements estimated in nano-slits [31,32]. The black dot-dashed line shows the arm length divided by the gap size, ℓ/g, with no fit parameters. This can serve as a rule of thumb for predicting antenna enhancement.

#161464 - $15.00 USD Received 13 Jan 2012; revised 21 Mar 2012; accepted 21 Mar 2012; published 28 Mar 2012
(C) 2012 OSA

Figure 5(d) shows the enhancement in the gap as a function of arm length when each antenna was driven by a multi-cycle THz pulse tuned to its frequency of maximum enhancement. Small imperfections in the antenna structures and variations in the multicycle THz waveforms at the different frequencies as well as limited S/N in the reflection measurements all contributed to scatter in the plot and a systematic disagreement between this data and the more reliable results in Fig. 5(c). These results, simulations, and transmission measurements [Fig. 4(b)] all indicate that, for a given gap size, the peak enhancement increases approximately linearly with length. This occurs because electrons from the entire length of the antenna are concentrated at the ends when excited on resonance, leading to more charge, and thus a larger field, in longer antennas. Again, the black dot-dashed line shows ℓ / g.

Our measurements have revealed key antenna features including the near-field spectral response, magnitude of the maximum field enhancement, and the time-dependent near-field profile in unprecedented detail. This will facilitate antenna design at all frequency ranges. Our methodology can also be applied to complex structures including metamaterials whose unique capabilities are based on near-field profiles and enhancements within antenna-like elements. In addition, enhancements of almost 40-fold and greater enhancements in future antennas with smaller gaps will enable new nonlinear THz phenomena to be explored. In spite of the fact that the enhanced field is tightly localized, the ability to probe exclusively in the gap region lets us take full advantage of the enhancement. High THz peak fields have been generated by other tabletop, ultrafast methods [33–35], but the THz output is typically a single-cycle pulse that has its energy distributed over a broad spectral range. The THz transients measured in our smallest antenna gaps have greater than 500 kV/cm peak-to-peak field strengths, comparable to those in strong single-cycle pulses. Our antenna-enhanced multicycle transients, however, have their energy concentrated in a much narrower spectral range, with spectral brightness exceeding that of the most intense broadband THz pulses. This spectral brightness makes it possible to strongly drive selected resonant transitions (electronic, vibrational, or rotational) for waveguide-based nonlinear spectroscopy and coherent control, while avoiding unwanted responses driven by extraneous frequency components. In the future, substantially larger *E*-fields could be produced by driving the antennas with stronger THz waves produced simply with additional optical pump pulse energy or with intensity-modulated optical pump waveforms tailored for efficient generation of multi-cycle THz pulses.

Appendix A: Sample preparation

The antennas, patterned by direct laser writing with a DWL 66 (Heidelberg Instruments), were deposited on a 30-μm $LiNbO_3$ substrate. First, a 1.4 μm thick layer of photoresist (AZ5214 E from Clariant Co.) was spin-coated onto the $LiNbO_3$. The sample was then scanned in the plane of the laser focus with the photoresist exposure calibrated appropriately for resist thickness and substrate. This allowed programmable patterning with ~1 μm resolution. After development and removal of the exposed photoresist [Fig. 6(a)], a 10 nm adhesion layer of chromium followed by a 150 nm layer of gold was evaporated on the photoresist and the patterned areas [Fig. 6(b)]. The final structure was achieved through a lift-off process [Fig. 6(c)]. Due to the negative wall profiles of patterned photoresist, the gold on AZ5214 E can be gently rinsed with acetone and removed without an ultrasonic process that could damage or crack the thin slab.

#161464 - $15.00 USD Received 13 Jan 2012; revised 21 Mar 2012; accepted 21 Mar 2012; published 28 Mar 2012
(C) 2012 OSA

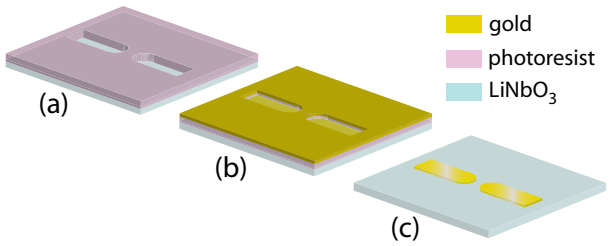

Fig. 6. Sample fabrication procedure. The optical lithography process for depositing 150 nm thick gold antennas on a 30 μm thick $LiNbO_3$ slab.

Appendix B: Ultrafast phase sensitive imaging

All experiments studying the interaction between THz waves and the gold antennas used ultrafast methods. Both the imaging experiments (Figs. 2 and 7) and single-point spectroscopy measurements (Figs. 3, 4, 5, and 8) were conducted with an amplified titanium-sapphire laser with a repetition rate of 1 kHz and a pulse duration of 80 fs. A beamsplitter separated pump and probe pulses, and the pump was delayed relative to the probe using a mechanical delay stage.

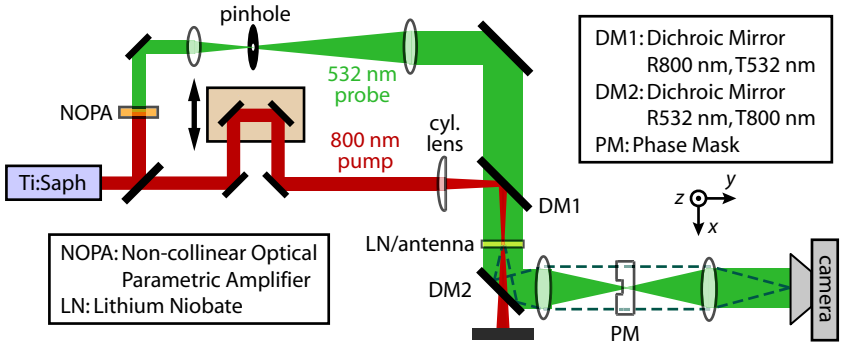

Fig. 7. The experimental geometry for time-resolved, phase contrast imaging of THz waves in the $LiNbO_3$ sample.

To study the antenna mode profile, we used time-resolved, phase-sensitive imaging [24–27]. The vertically polarized pump generates a vertically polarized THz wave that is wave-guided down the thin $LiNbO_3$ slab. The THz electric field changes the $LiNbO_3$ index of refraction via the electro-optic effect. A spatially expanded, vertically polarized probe beam is routed through the sample (see Fig. 7), where it accumulates a spatially varying phase shift due to the THz-induced change in index: $\Delta\phi(y,z) \propto \Delta n(y,z) \propto E_{\mathrm{THz}}(y,z)$. In this setup, the index change depends only on the z (vertical) component of the THz E-field. Because the camera detects intensity, a phase-sensitive imaging technique is required to observe the phase shift. We used phase contrast imaging [26,27]. In the back focal plane of the first lens after the sample, i.e. the Fourier plane, the light diffracted off the THz wave is spatially separated from the principal, undiffracted beam. In that plane, a mask (a flat plate with a 25 μm x 25 μm recessed region) introduces a $\pi/2$ phase shift between the principal beam and the diffracted light. When the principal beam and the diffracted light subsequently recombine in the image plane, they interfere to make an amplitude image that is detected by the camera. By changing the time delay between pump and probe, a series of images can be recorded and compiled into a video clip showing the propagation of the THz wave (see Media 1 and Media 2).

We used a non-collinear optical parametric amplifier (NOPA) to generate 80 fs probe pulses at 532 nm. A spectral bandpass filter before the camera transmitted the 532 nm probe light but blocked the 800 nm pump light and 400 nm light resulting from second harmonic

#161464 - $15.00 USD Received 13 Jan 2012; revised 21 Mar 2012; accepted 21 Mar 2012; published 28 Mar 2012
(C) 2012 OSA

generation in the $LiNbO_3$ sample. To facilitate tight focusing of the principal probe beam at the phase mask and high-resolution imaging, the first lens after the $LiNbO_3$ sample was an aplanatic lens with a numerical aperture of 0.15, resulting in an image resolution better than 2 μm.

Appendix C: Spectroscopy in reflection and transmission geometries

In order to perform careful spectroscopy of the antennas, we switched from imaging to point source detection, which greatly enhanced the signal to noise ratio (S/N) and enabled reflection measurements. To generate broadband THz waves for spectroscopy, such as those shown in Figs. 3(a)–3(c), the pump was focused to a line (~1 cm tall, 30 μm wide, 100 μJ pulse energy) in a $LiNbO_3$ sample [26]. For quantitative measurement of *E*-field and antenna enhancement, multi-cycle, "narrowband" THz waves tuned to the antenna resonance were preferred over broadband THz waves [see Fig. 3(d)]. Pumping the antennas on resonance increased the peak *E*-field enhancement and the spectral amplitude of the signal for improved S/N in reflection mode measurements. Because of waveguide dispersion, different THz frequencies propagate at very different velocities, so a tilted intensity front in the optical pump pulse can be used to velocity match, and thus coherently amplify a single THz frequency [21]. The tilted pump pulse for narrowband THz waves was prepared by imaging a diffraction grating onto the sample (see Fig. 8), with the tilt angle controlled by changing the magnification of the imaging system. We used 1 mJ pump pulse energy with a spot size at the sample of ~5 mm wide and 300 μm tall. The two pumping geometries complement each other in that the broadband THz pulse can be used to scan a wide frequency range and determine the resonant frequencies of the first several antenna modes in a single measurement. The narrowband pulse can then be tuned to the resonant frequency of the antenna to measure field enhancement and characterize the resonant response.

To fully characterize the THz fields, it was necessary to focus the probe tightly enough that it could fit into a 2 μm antenna gap and to position the probe relative to the antenna with sub-micrometer accuracy. It also was beneficial to make both optical transmission measurements, which have the excellent S/N required for broadband spectroscopy, and optical reflection measurements, which enable quantitative determination of THz *E*-fields at the surface of the $LiNbO_3$ crystal where the gold antenna was deposited. This was important because the THz field is not uniform throughout the $LiNbO_3$ thickness for two reasons. First, the $LiNbO_3$ slab acts like a planar THz waveguide, and while the lowest-order waveguide mode that predominates far from any antenna structure is fairly uniform as a function of depth in the crystal, the higher-order modes that are weakly excited are not. Second, in the antenna's near-field, the THz fields vary on micron and sub-micron length scales as a function of both depth and lateral position. As a result, the field profile and enhancement in the antenna gap cannot be quantitatively characterized by averaging over the $LiNbO_3$ crystal thickness, thus necessitating reflection measurements. The experimental setup in Fig. 8 enables tight focusing and high-precision positioning of the probe beam and switching between transmission and reflection mode without adjusting the sample or any beam-steering optics.

In this setup, 800 nm light in the probe arm is frequency-doubled to 400 nm in a β-BBO crystal. The 400 nm light is spatially filtered and expanded to make a Gaussian beam with a diameter designed to back-fill the objective used to focus the probe onto the sample. To prevent sample damage by the tightly focused probe, the beam is attenuated to less than 1 nJ/pulse. After a polarizer, which is used to control the polarization state in transmission and reflection measurements, 20% of the probe beam is reflected off the beamsplitter (BS2). This light is then transmitted through a dichroic mirror and focused onto the sample with an 0.28 numerical aperture, 3.3 cm working distance objective lens, resulting in a 1 μm probe spot at the $LiNbO_3$ surface.

In addition to the 400 nm probe light, incoherent, 530 nm light from a light emitting diode (LED) is incident on the sample from the back side. The sample is imaged onto the camera,

#161464 - $15.00 USD Received 13 Jan 2012; revised 21 Mar 2012; accepted 21 Mar 2012; published 28 Mar 2012
(C) 2012 OSA

and the objective used to focus the probe is the first lens in this imaging system, yielding 1 μm imaging resolution. In addition to the incoherent light being imaged onto the camera, a small fraction of 400 nm probe light reflected from the sample surface (~10%) is also reflected from the 532 nm reflecting dichroic mirror, and imaged onto the camera. The image on the camera shows the antenna structure and the 1 μm probe spot. The sample is mounted on a 3-dimensional translation stage with differential micrometers, allowing positioning relative to the probe spot with ~200 nm accuracy. Figure 2(b) shows the probe accurately positioned in the middle of a 5 μm antenna gap. After the sample was correctly positioned, the LED was shut off to prevent extraneous light from hitting the photodiodes during pump-probe measurements.

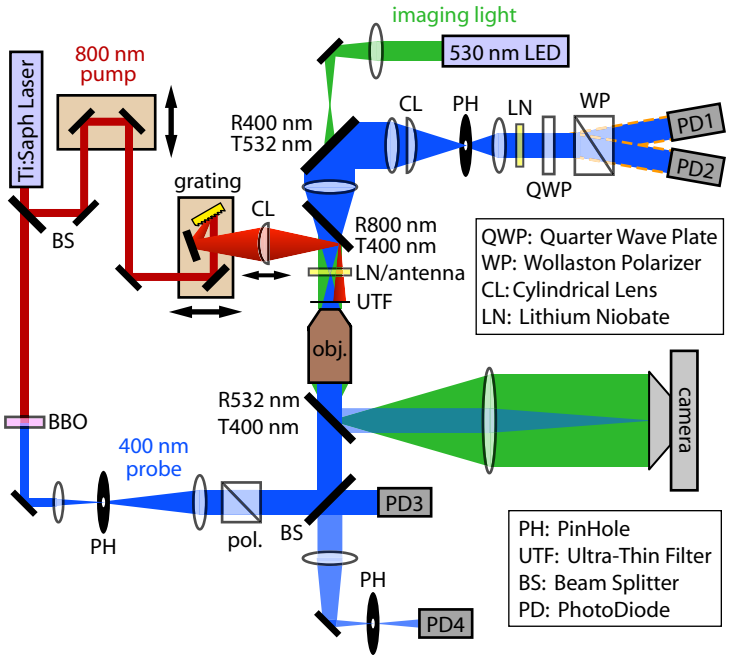

Fig. 8. The experimental geometry for point-source detection. The sample is imaged onto the camera using incoherent 530 nm light from an LED source. A small fraction of the 400 nm probe light also reaches the camera, allowing simultaneous visualization of antenna and probe spot. The sample is mounted on a 3D translation stage with differential micrometers, making it possible to position the sample with ~200 nm accuracy relative to the probe spot which is focused to 1 μm with a 0.28 numerical aperture microscope objective [see Fig. 2(b)]. After the sample is correctly positioned, the THz transients can be measured in transmission or reflection mode. The intensity front of the optical pump pulse is tilted by imaging a diffraction grating onto the sample.

After correctly positioning the pump, probe, and sample, optical transmission or reflection mode measurements could be made without changing alignment. For both transmission and reflection measurements, the pump was chopped at 500 Hz and the signal was detected at the modulation frequency using a data acquisition (DAQ) card [36]. Balancing was implemented between photodiodes PD1 and PD2 for transmission and between PD3 and PD4 for reflection (see Fig. 8). The overall minimum signal detection threshold was $\Delta I / I_0 \sim 10^{-4}$.

Transmission was used for broadband THz measurements because of the excellent S/N. To correctly implement transmission measurements, it is necessary to control the beam collimation. After passing through the sample, the transmitted probe beam is rapidly diverging. Before being collimated, it passes through a R800 nm/T400 nm dichroic mirror angled at 45°, which changes the apparent location of the focus for divergence along the

#161464 - $15.00 USD Received 13 Jan 2012; revised 21 Mar 2012; accepted 21 Mar 2012; published 28 Mar 2012
(C) 2012 OSA

horizontal and vertical directions. A cylindrical lens (see Fig. 8) corrects for this, and makes it possible to focus the probe to ~100 μm and later to collimate the beam. The pinhole was necessary to block 400 nm light that was generated through second harmonic generation of the pump light in the $LiNbO_3$ sample, which could not be rejected by a spectral filter like the 800 nm pump light.

In transmission mode, the THz signal was encoded as a change in the polarization state of the probe. The probe polarization was initially set to 45°, and the THz induced a change in the relative index between vertically and horizontally polarized light in the $LiNbO_3$. The change in relative index was encoded as a phase shift, $\Delta\varphi$, between the vertical and horizontal components. The final quarter wave plate (which changes the 45° polarized light to circularly polarized light) and Wollaston polarizer convert the phase shift to an amplitude shift. The signal detected at the photodiodes is (for ideal optics):

$$I_0(1 \pm \sin\Delta\varphi), \tag{1}$$

where the "+" corresponds to PD1 and the "–" to PD2. Subtracting the output of the two diodes doubles the signal and suppresses common mode noise. The second slab of $LiNbO_3$, located just before the quarter wave plate, is rotated 90° relative to the sample to correct for the inherent, static birefringence of the $LiNbO_3$ sample. Additional adjustment is needed to correct for the depolarizing effects of the beamsplitter and three dichroic mirrors between the two polarizers that reflect or transmit the probe. These optics affect the relative amplitudes of vertical and horizontal polarization components and introduce a static phase shift between these components. Jones matrix analysis [37] shows that the amplitude change can be corrected by rotating the input polarizer away from 45°, and the static phase shift can be corrected by tilting the quarter wave plate so that it induces a phase shift greater than 90°. After making these corrections, we observe a nearly ideal polarization state after the quarter wave plate, and can use Eq. (1) to quantitatively extract the THz-induced phase shift.

The THz-induced phase shift is directly proportional to the THz electric field, with the proportionality constant determined by the electro-optic effect. Taylor expanding Eq. (1) in $\Delta\varphi$ gives [27]

$$\frac{\Delta I}{I_0} \approx 2\Delta\varphi = 4\pi\frac{\ell}{\lambda_{\text{opt}}}\left\langle \Delta n_{eo} - \Delta n_o \right\rangle = 2\pi\frac{\ell}{\lambda_{\text{opt}}}\left(r_{33}n_{eo}^3 - r_{13}n_o^3\right)\left\langle E_{\text{THz}}\right\rangle, \tag{2}$$

where ℓ is the $LiNbO_3$ slab thickness, λ_{opt} is the free space optical wavelength, Δn_{eo} and Δn_o are the THz-field-induced changes in refractive index for the extraordinary and ordinary axis, respectively, r_{33} and r_{13} are the appropriate electro-optic coefficients, and $\left\langle E_{\text{THz}}\right\rangle$ is the average z-component of the THz electric field experienced by the probe as it propagates through the crystal. Transmission mode has very strong signals (typical peak $\Delta I / I_0$ is 20%), and in an unmodified dielectric slab waveguide the effect of averaging the THz E-field through the crystal depth can be calculated analytically [27] and used to quantitatively determine the peak E-field. The antenna, however, strongly localizes the electric field, and averaging through the crystal depth prevents accurate quantitative measurement of enhancements in the near-field region of the gap.

To measure the THz electric field at the surface where the antenna is deposited, reflection mode measurements are required. For reflection measurements, the 400 nm probe is polarized vertically, parallel to the THz polarization, the optic axis of the $LiNbO_3$ crystal, and the long axis of the antenna. Of the probe light that is incident on the $LiNbO_3$ crystal, about 14% is reflected off the front surface, and this is collected and collimated by the same objective lens used to focus the probe. The majority of this reflected light is transmitted through the dichroic mirror (R532 nm/T400 nm) and beamsplitter (BS2) and detected by photodiode PD4 (see Fig. 8).

#161464 - $15.00 USD Received 13 Jan 2012; revised 21 Mar 2012; accepted 21 Mar 2012; published 28 Mar 2012
(C) 2012 OSA

At normal incidence, the reflection off a dielectric interface is given simply by $R = (n_2 - n_1)^2 / (n_1 + n_2)^2$. Given that the vertically polarized optical probe is incident from free space, then, the signal modulation after Taylor expansion in Δn_{eo} is

$$\frac{\Delta R}{R_0} \approx \frac{4\Delta n_{eo}^{\text{surf}}}{n_{eo}^2 - 1} = \frac{2 r_{33} n_{eo}^3}{n_{eo}^2 - 1} E_{\text{THz}}^{\text{surf}}. \tag{3}$$

Here $E_{\text{THz}}^{\text{surf}}$ is the *z*-component of the THz electric field at the surface of the $LiNbO_3$ slab. Because fields parallel to a dielectric interface must be continuous, this measurement reports directly on the *E*-field in the antenna gap and can be used to quantify field enhancement.

In reality, reflection measurements report on the index change not exclusively at the surface but also in a subwavelength region beneath it. Eq. (3) assumes that Δn_{eo} is uniform throughout this region, so strong THz field gradients at the surface could invalidate this assumption. To confirm that the non-uniform THz field profile has a negligible effect on ΔR, we calculated the reflectivity for a material with a depth-dependent induced change in index [38]. The amplitude reflection coefficient (Eq. (32) from [38] after substitution of variables) is given by

$$r = r_0 + \frac{i4k}{(n_{eo} + 1)^2} \int_0^\infty \exp(2ikx) \Delta n_{eo}(x) dx \equiv r_0 + \Delta r \tag{4}$$

with *k* the optical wave vector in the $LiNbO_3$ and $r_0 = (1 - n_{eo}) / (1 + n_{eo})$ the reflectivity from the dielectric interface in the absence of a THz field. We assume the field decays exponentially away from the surface: $\Delta n_{eo}(x) = \Delta n_{eo}^{\text{surf}} \exp(-x / l)$. Evaluating the integral in Eq. (4), calculating $\Delta R / R_0$ using $R = |r|^2$, and keeping only terms that are first order in Δn yields

$$\frac{\Delta R}{R_0} = \frac{1}{1 + [\lambda_{\text{opt}} / (4\pi n_{eo} l)]^2} \frac{4\Delta n_{eo}^{\text{surf}}}{n_{eo}^2 - 1}, \tag{5}$$

which can be compared directly with Eq. (3). The signal strength is not attenuated appreciably relative to Eq. (3) so long as $l >> \lambda_{\text{opt}} / (4\pi n_{eo}) = 14$ nm. Because we expect the decay length of the THz field to be on the order of the gap size, for the gaps in this paper *l* is far larger than c14 nm and $\Delta R / R_0$ is accurately predicted by Eq. (3).

A drawback of reflection measurements is that reflection mode signals ($\Delta R / R_0$) are roughly 700-fold weaker than transmission mode signals ($\Delta I / I_0$), as can be seen by comparing Eqs. (2) and (3). This reduction in S/N makes it difficult to perform broadband spectroscopy in reflection mode. An additional drawback of reflection mode measurements is that the beam has contributions from reflections off both the front and back surfaces of the $LiNbO_3$ slab, but the enhanced electric fields are localized at the front surface where the antenna is deposited. To eliminate the reflection off the back surface of the slab, the reflected probe beam was focused through a 15 μm pinhole with a 30 cm focal-length lens. In addition to excluding the reflection off the back surface, the pinhole also blocked 400 nm pump light. When the pinhole was translated along the direction of beam propagation, the reflections off of both surfaces could be clearly observed 5 mm apart, as predicted by Gaussian beam analysis [39]. When the pinhole was correctly positioned to optimally transmit the reflection off the front surface, the back surface reflection was attenuated by ~15-fold, effectively eliminating its contribution to the enhanced signal in the antenna gap. As a control, the probe polarization was rotated 90° to horizontal. The reflection signal was reduced by a factor of ~3

#161464 - $15.00 USD Received 13 Jan 2012; revised 21 Mar 2012; accepted 21 Mar 2012; published 28 Mar 2012
(C) 2012 OSA

as predicted by the electro-optic effect ($\Delta n_{eo} / \Delta n_o = r_{33} n_{eo}^3 / r_{13} n_o^3 = 3.1$), indicating that the signal was accurately described by Eq. (3).

When capturing reference scans, in which there was no field enhancement at the front surface, the pinhole's 15-fold attenuation was not sufficient to completely suppress the contribution from the back surface reflection, which was strongly modulated by the THz during its round-trip through the sample. To measure the reference scan, we recorded the THz time trace in transmission mode. Rearranging Eq. (2), the electric field at the surface in a plain, unstructured slab waveguide is given by:

$$E_{\mathrm{THz}}^{\mathrm{surf}} = \frac{\xi_{\mathrm{THz}}^{\mathrm{surf}}}{\langle \xi_{\mathrm{THz}} \rangle} \langle E_{\mathrm{THz}} \rangle = -\frac{1}{2\pi (r_{33} n_{eo}^3 - r_{13} n_o^3)} \frac{\lambda_{\mathrm{opt}}}{\ell} \frac{\xi_{\mathrm{THz}}^{\mathrm{surf}}}{\langle \xi_{\mathrm{THz}} \rangle} \frac{\Delta I}{I_0}, \tag{6}$$

where $\xi_{\mathrm{THz}}^{\mathrm{surf}} / \langle \xi_{\mathrm{THz}} \rangle$ is the ratio between the *E*-field amplitude at the crystal surface and the average *E*-field experienced by the probe as it passes through the crystal. Because the mode structure in a planar waveguide is well known, $\xi_{\mathrm{THz}}^{\mathrm{surf}} / \langle \xi_{\mathrm{THz}} \rangle$, which is on the order of 1, can be determined analytically as a function of mode and frequency [27]. This correction can be applied in the Fourier domain to quantitatively determine spectral amplitudes at the surface of a plain waveguide from a transmission mode setup. To confirm the ability to quantitatively measure surface fields in transmission mode, we recorded reflection and transmission scans in a plain waveguide and used Eqs. (3) and (6) respectively to calculate $E_{\mathrm{THz}}^{\mathrm{surf}}$. To eliminate the contribution from the back surface in the reflection measurement, we used a longer focal length lens before the 15 μm pinhole to increase the attenuation of the back surface reflection. In addition, we coated the back surface of the $LiNbO_3$ slab with nail polish, which served as a simple antireflection coating since its index was intermediate between $LiNbO_3$ and air. A scan of the pinhole confirmed that a negligible amount of light from the back surface made it through the pinhole. Measurements of peak $E_{\mathrm{THz}}^{\mathrm{surf}}$ calculated with the two methods differed by ~10%, confirming the ability to use transmission scans for reference measurements. Transmission mode reference measurements were used to record the blue trace in Fig. 3(d) and for determining field enhancements in Fig. 5(c) and 5(d).

Appendix D: Modeling the antenna as a damped driven harmonic oscillator

As mentioned in the main text of the paper, the line shape can be understood qualitatively by modeling the antenna as a damped driven harmonic oscillator. The amplitude of the *E*-field in the antenna gap should be proportional to the amount of charge built up at the antenna ends. The differential equation describing the charge is:

$$\frac{d^2 Q}{dt} + 2(2\pi\nu_0)\gamma \frac{dQ}{dt} + (2\pi\nu_0)^2 Q = (2\pi)^2 A_0 \sin(2\pi\nu t). \tag{7}$$

Here ν is the driving frequency, ν_0 is the undamped resonant frequency, and γ is the damping ratio. The well-known solution (ignoring transients) is a harmonic response at the driving frequency with a driving frequency dependent amplitude and phase:

$$Q(t) = A(\nu) \sin[2\pi\nu t + \phi(\nu)] \tag{8a}$$

$$A(\nu) = \frac{A_0}{\sqrt{(2\nu\nu_0\gamma)^2 + (\nu^2 - \nu_0^2)^2}} \tag{8b}$$

#161464 - $15.00 USD Received 13 Jan 2012; revised 21 Mar 2012; accepted 21 Mar 2012; published 28 Mar 2012
(C) 2012 OSA

$$\varphi(\nu) = \arctan\left(\frac{2\nu\nu_0\gamma}{\nu^2 - \nu_0^2}\right). \tag{8c}$$

The amplitude and phase are plotted in the Fig. 9(a) with γ = 0.18. The amplitude has a DC response, peaks at $\nu_{max} = \nu_0\sqrt{1-2\gamma^2}$ (slightly lower in frequency than the undamped resonance), and decays to zero at high frequencies. The response is in phase with the driving field at very low frequencies, phase shifted by -π/2 at ν_0, and out of phase at high frequencies [see red trace in Fig. 9(a)].

Because the signal strengths were too weak to measure the broadband response in reflection mode, we recorded these spectra in transmission mode as described above. As a result, the measured near-field signal interferes with a background accumulated as the probe travels through the depth of the crystal. The measured signal is approximately the near-field signal plus the reference signal: $E_{sig}(\nu) \approx E_{nf}(\nu) + E_{ref}(\nu)$. The traces plotted in Figs. 3 and 4 are $\left|\frac{E_{sig}(\nu)}{E_{ref}(\nu)}\right| \approx \left|\frac{E_{nf}(\nu)}{E_{ref}(\nu)} + 1\right|$, where $\frac{E_{nf}(\nu)}{E_{ref}(\nu)}$ is a measure of the antenna response. Figure 9(b) shows the in-gap signal for a 110 μm arm-length antenna from Fig. 4(b) and $|Q(\nu)+1|$ with ν_0 = 0.24 THz, γ = 0.18, and A_0 = 0.14. The characteristics of the spectrum are predicted fairly well, including the DC response, the enhancement peak, and a minimum above the resonance. The minimum results from destructive interference between the near-field signal, which is out-of-phase with the driving field, and the background signal. At frequencies greater than the minimum (above ~0.45 THz), the data is complicated by the higher order antenna modes, so it is probable that the response from the lowest mode decays away as predicted. It is possible to capture many of the high-frequency features in the spectrum by including additional resonances in the model. One feature not completely explained is the observed frequency difference between the enhancement maximum and the transmission minimum, which is significantly greater than the red shift between the enhancement maximum and the undamped resonant frequency in the model [vertical dashed line in Fig. 9(b)]. In spite of this difficulty, thinking of an antenna as a damped harmonic oscillator with charge driven by the input wave provides excellent intuition for antenna behavior.

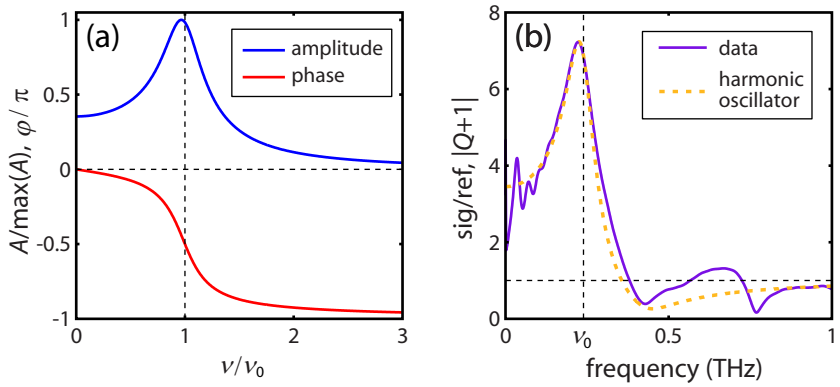

Fig. 9. Modeling the antenna as a damped harmonic oscillator. (a) The amplitude and phase of a damped harmonic oscillator (γ = 0.18) as a function of the normalized driving frequency, ν/ν_0, with ν_0 the resonant frequency. (b) The experimentally measured enhancement in the gap of a 110 μm arm-length antenna (purple) and $|Q + 1|$, the interference between the harmonic oscillator response and a constant background (orange).

#161464 - $15.00 USD Received 13 Jan 2012; revised 21 Mar 2012; accepted 21 Mar 2012; published 28 Mar 2012
(C) 2012 OSA

Acknowledgments

We thank Alex Maznev for helpful discussions. This work was supported by NSF grant no. ECCS-0824185, ONR grant no. N00014-09-1-1103, AFOSR grant no. FA9550-09-1-0708, and DTRA sub-contract W911NF-06-2-0040. C. W. was supported in part by an NSF GRFP fellowship.

#161464 - $15.00 USD Received 13 Jan 2012; revised 21 Mar 2012; accepted 21 Mar 2012; published 28 Mar 2012
(C) 2012 OSA